Journal of Materials Chemistry A

Designing interconnected passages by "legs-to-head" directional U-shape freeze casting to boost solar-driven self-pumping oil spill recovery

Journal:	*Journal of Materials Chemistry A*
Manuscript ID	TA-ART-11-2023-007164.R1
Article Type:	Paper
Date Submitted by the Author:	16-Apr-2024
Complete List of Authors:	Wu, Shiwen; The University of Texas at Dallas, Mechanical Engineering Mashhadian, Amirarsalan; The University of Texas System, The University of Texas at Dallas Jian, Ruda; The University of Texas at Dallas, Mechanical Engineering Tian, Siyu; The University of Texas at Dallas, Mechanical Engineering Luo, Tengfei; University of Notre Dame, Aerospace and Mechanical Engineering Xiong, Guoping; The University of Texas at Dallas, Mechanical Engineering

Designing interconnected passages by "legs-to-head" directional U-shape freeze casting to boost solar-driven self-pumping oil spill recovery

Shiwen Wu[1], Amirarsalan Mashhadian[1], Ruda Jian[1], Siyu Tian[1], Tengfei Luo[2], Guoping Xiong[1,*]

[1.] Department of Mechanical Engineering, The University of Texas at Dallas, Richardson, Texas 75080, USA

[2.] Department of Aerospace and Mechanical Engineering, University of Notre Dame, Notre Dame, Indiana 46556, USA

* Corresponding author: Guoping Xiong: guoping.xiong@utdallas.edu

Abstract

Solar-heating siphon-assisted oil recovery is promising as an eco-friendly strategy for oil spill mitigation due to its spontaneous, continuous, and renewable operation. However, the slow oil transport rate has constrained its progression. Here, we report a novel "legs-to-head" directional U-shape freeze casting method to fabricate siphon-assisted oil skimmers with well-aligned channels in the "legs" and interconnected pathways in the "head" to enhance the oil recovery rate. Real-time temperature monitoring during freezing clarified the influence of the connecting angle between the "legs" on the channel structure within the "head". Resulting from a balance between the transport barrier in the "head" and the flow resistance in the "legs" of the oil skimmers, optimal performance was achieved at a 60° connection angle between the "legs", yielding a high oil recovery rate of 620.2 L m^{-2} h^{-1} under 1-sun irradiation. Furthermore, the outdoor test demonstrated a peak rate of 938.2 L m^{-2} h^{-1} at noon and a remarkable daily collection of 14,001 L m^{-2}, achieved without external power or human intervention. Notably, the oil flow flux is calculated to be 207,218 L m^{-2} h^{-1} bar^{-1}, outpacing conventional pump-assisted devices. This work provides pioneering designs towards efficient oil spill remediation and other fluid transport applications.

Keywords

U-shape directional freeze casting; siphon effect; oil transport; solar-heating effect; self-pumping

1. Introduction

Frequent oil leakage accidents during offshore oil exploration and marine transportation have resulted in substantial losses of valuable oil resources and severe damage to marine ecosystems[1–4], underscoring a dire need for advanced and effective oil spill recovery solutions. Physical absorption based on materials with selective wettability (oleophilic yet hydrophobic) offers an eco-friendly method to recycle oil sources from oil-contaminated wastewater[4–8]. This method differs from conventional methods such as *in situ* combustion[9], bioremediation[10], chemical interventions[11], and oil containment booms[12,13]. Specifically, two primary strategies characterize physical absorption-based oil recovery. The first one is constructing filtration-type oil collectors using oleophilic/hydrophobic membranes[14–17] or membranes featuring underwater superoleophobicity[18,19] as the filter. These membranes allow oil to pass through while rejecting water, thus achieving oil/water phase separation. However, as oil/water separation progresses, accumulated water droplets obstruct the membrane pores, which impedes continuous operation. The second strategy is *in situ* oil collection from water surfaces driven by external forces[20–24]. While this method ensures continuous oil recovery, it demands energy-consuming post-treatments, such as pumping[25] and squeezing[26], thereby increasing operational complexities.

A new strategy in this domain involves oil skimmers based on the siphon effect[27–29]. Such skimmers employ capillary adsorption for self-starting oil recovery, transporting oil from polluted sites to collecting containers using just gravitational energy. Unlike the conventional physical absorption strategies, siphon-assisted oil skimmers eliminate the need for external

power sources or manual interference, enabling direct oil recovery from oil-contaminated wastewater in a spontaneous, continuous, low-cost, and environmentally friendly manner. However, a challenge with siphon-assisted oil skimmers lies in their relatively low oil transport rate (generally ~ 100 L m^{-2} h^{-1})[27–29], especially when compared with other pump-assisted devices (e.g., 500-600 L m^{-2} h^{-1})[21,25].

The flow behavior of liquids driven by siphon effects is critically dependent on the channel structure[27,30,31]. Consequently, there is an urgent demand for innovative channel designs to improve the oil transport rates of siphon-assisted oil skimmers. Directional freeze casting offers a promising solution, which is known for its effectiveness in crafting low-tortuosity and aligned channels to facilitate liquid transport[32–35]. This method involves directional solidification of a suspension along a controlled temperature gradient, followed by the sublimation of the solidified solvent (e.g., water) to yield a well-shaped three-dimensional (3D) monolith mirroring the negative imprint of the ice[36–38]. However, designing channels for siphon-assisted oil skimmers is complex due to their inherent U-shape structure, particularly at the highly curved juncture where two “legs” of the U-shape converge. Rapid oil transport in these U-shaped skimmers relies heavily on the strategic design of channel structures, especially at this critical juncture.

In this study, we introduce a new design for siphon-assisted oil skimmers with interconnected well-aligned graphene channel structures, denoted as well-aligned oil skimmers (WOS). These are crafted through a specialized “legs-to-head” directional U-shape freeze casting process (LHFC), as illustrated in Figure 1. The freezing process of graphene solution

is carefully manipulated to start from both ends of the U-shaped "legs", converging ultimately in the "head" region. We find that the channel structure within the "head" is critically contingent upon the connection angle (θ) between the two "legs". At $\theta = 0°$, channels in the "head" remain isolated from each other and align perpendicularly to the direction of oil flow. As a result, oil skimmers developed via directional freeze casting even underperform in comparison to those crafted through random freeze casting at $\theta = 0°$. In contrast, at $\theta = 60°$, channels formed in the "legs" coalesce into an interconnected network in the "head" region. This interconnection substantially lowers the transport barriers in the "head", accelerating oil transport across the skimmers. Enhanced by the significant reduction in oil viscosity attributed to the exceptional solar-heating capability of graphene, the WOSs achieve a high oil recovery rate of 620.2 L m^{-2} h^{-1} under 1-sun irradiation (i.e., solar flux of 1 kW m^{-2}). Furthermore, outdoor field tests exhibit a peak oil recovery rate of 938.2 L m^{-2} h^{-1} at noon, with a cumulative daily yield of 14,001 L m^{-2} and an annual yield of 32,143 barrels m^{-2}. Remarkably, the WOS outperforms even pump-assisted oil recovery systems, demonstrating its substantial promise for practical, electricity and labor-independent oil spill remediation applications.

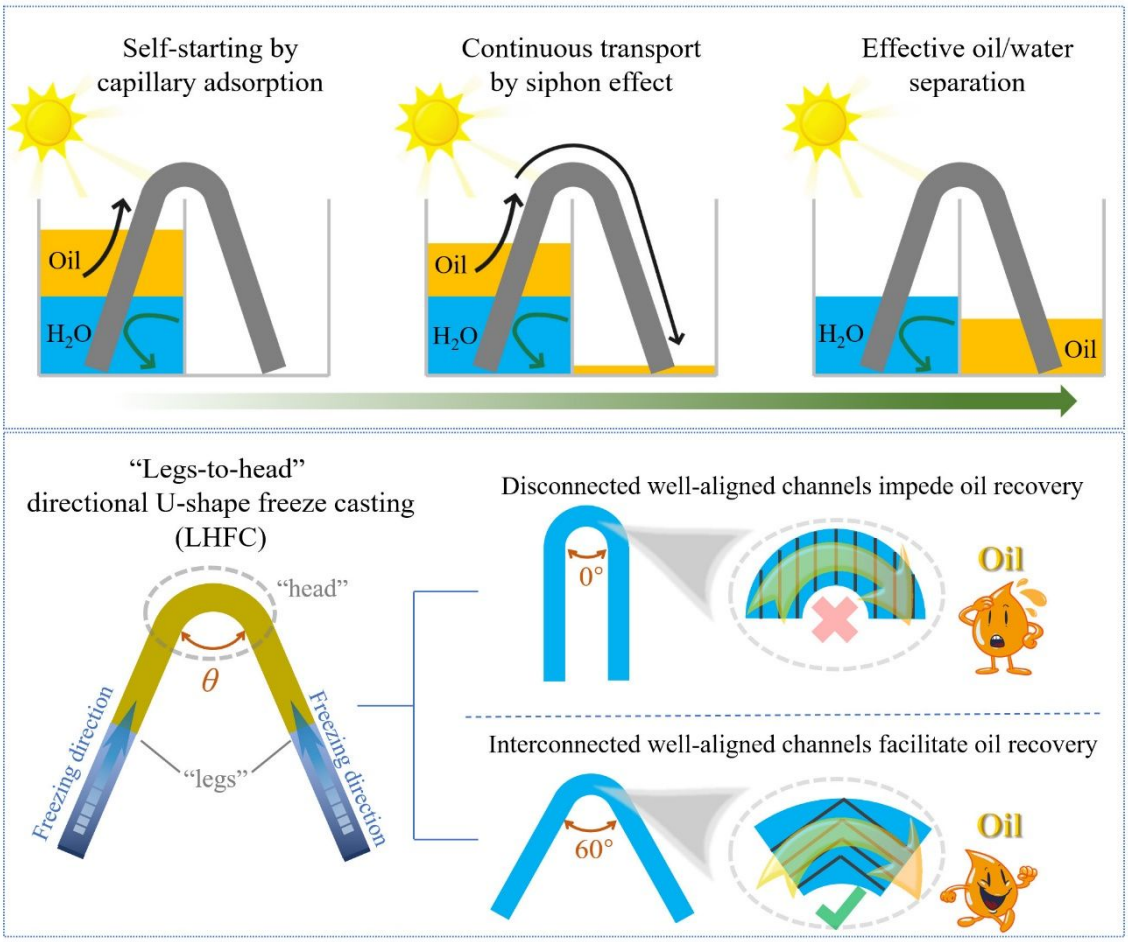

Figure 1. Schematic representation of the LHFC design for solar-heating siphon-assisted oil recovery. Channels in the "head" of WOS with $\theta = 0°$ are disconnected, impeding oil recovery, while the well-aligned channels in WOS with $\theta = 60°$ are interconnected in the "head", promoting rapid oil recovery.

2. Results and Discussion

2.1. Materials characterization

U-shape WOSs with various connection angles were prepared through an LHFC process with details described in Supplementary Materials. In brief, specific volumes of graphene oxide (GO) solutions were introduced into a 3D-printed U-shaped mold. During the LHFC process, the solidification of the GO solutions initiated from both ends of the U-shaped "legs", as

illustrated in Figure 2a. Following a vacuum drying process and subsequent thermal annealing, 3D graphene monoliths were obtained. To augment the solar absorption capability, vertically-standing graphene petals (GPs) were grown on the surface of graphene monoliths using plasma-enhanced chemical vapor deposition[27,28,39]. Each WOS is denoted based on its connection angle, θ, between the two "legs" of U-shaped oil skimmers. For instance, WOS-60 implies a connection angle of 60°. For comparison, oil skimmers with a randomized pore configuration (ROS) were constructed using similar procedures but frozen directly in a chilled condition at approximately -150℃. The concentration of GO solutions significantly affects the microstructure, wettability, and oil recovery performance of the fabricated WOS-60s, as demonstrated in Supplementary Figure S1. For this study, the GO concentration used to fabricate the oil skimmers is fixed as 10 mg/mL unless otherwise mentioned. Cross-sectional scanning electron microscope (SEM) images in Figure 2b present the morphology of the WOSs' two "legs" (highlighted in the inset) along the solidification trajectory, revealing prominent well-aligned channels spanning several tens of microns. Conversely, ROSs display a chaotic porous structure (Figure 2c) due to the uncontrolled solidification direction.

The oleophilic and hydrophobic characteristics of graphene[34] make WOSs naturally suited for selective oil extraction from contaminated wastewater. As demonstrated in Figure 2d and Supplementary Figure S2, oil droplets permeate the WOSs quickly, while water droplets remain on the surface, exhibiting a contact angle of 135°. Furthermore, the oil transport efficiencies of WOSs and ROSs were assessed using a customized oil-wicking test setup (Supplementary Figure S3). Corresponding mineral oil masses per area wicked by the "leg"

section in different skimmers were measured and plotted as a function of time, as shown in Figure 2e. The oil-wicking rates of WOSs substantially surpass those of ROSs, demonstrating the advantages of the low-tortuosity and well-aligned channels within the "legs" of WOSs. Moreover, the WOSs exhibit outstanding light-absorption properties across the entire solar spectrum (Figure 2f). Upon decorating GPs on the surface (Supplementary Figure S4), the overall solar absorption of WOSs jumps from 82.9% to 98.9%, which is attributed to the light-trapping effect of the vertically standing GPs[39–41]. Moreover, the maximum stress of WOSs increases from 1.6 kPa to 53.8 kPa as the applied compressive strain rises from 10% to 90% (Supplementary Figure S5), exhibiting good mechanical properties. At a compressive strain of 70%, the stress/density ratio of the WOSs reaches 3,505 Pa/(mg/cm^3), which is comparable to or even exceeds those of graphene aerogels reported in prior studies[34,42,43].

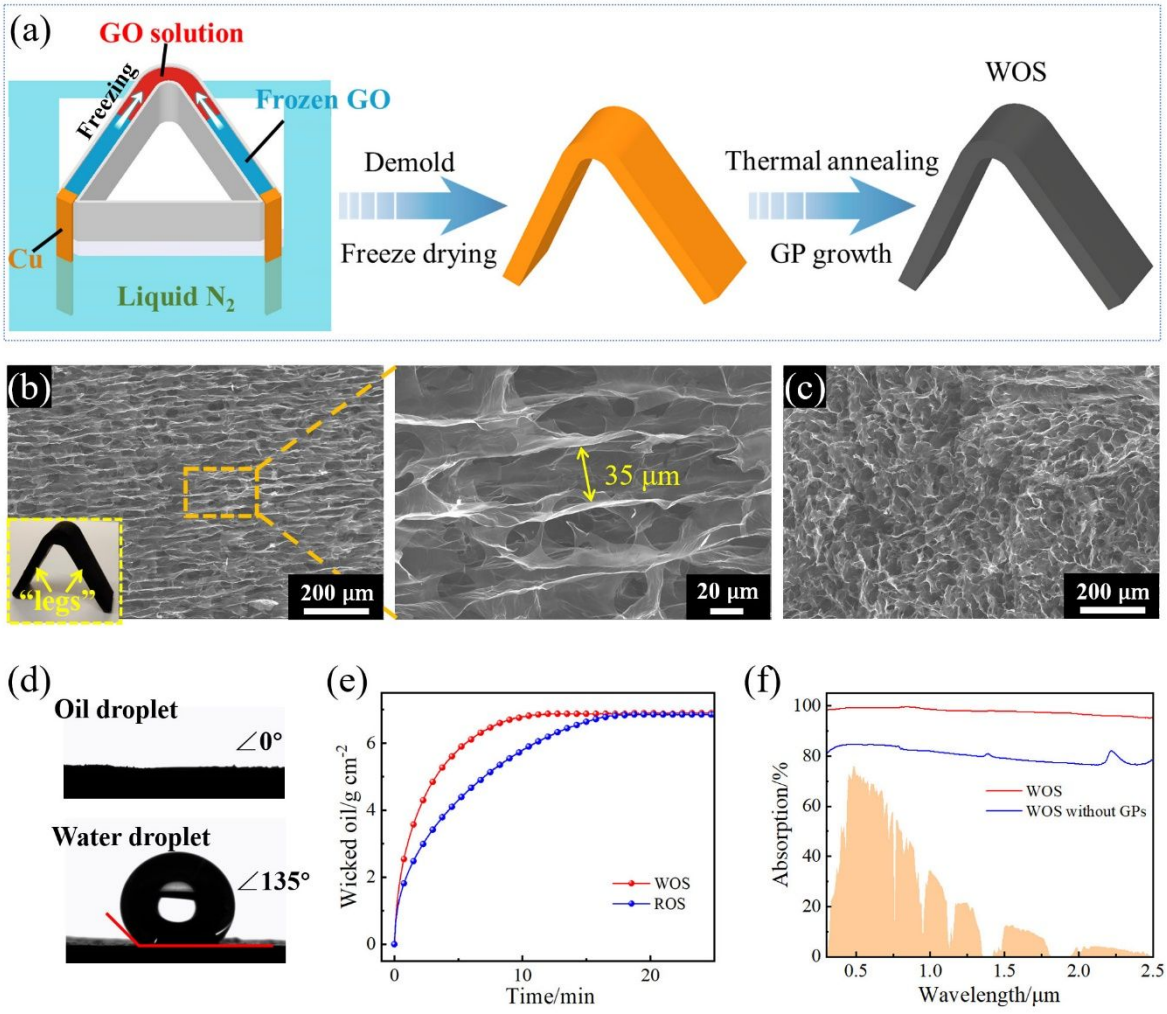

Figure 2. (a) Schematic illustrating the fabrication process of WOSs. (b-c) SEM images depict the cross-sectional morphology of the "legs" for (b) WOS and (c) ROS. Inset in (b) shows the photograph of WOS-60. (d) Mineral oil and water contact angle measurements for WOS. (e) Capillary rises of mineral oil against gravity over time in the "legs" of WOS and ROS. (f) Solar absorption spectra of WOSs before and after GP growth.

2.2. Indoor oil recovery performance of WOS-60

The oil recovery performance of WOSs is evaluated in a laboratory-scale experimental setup. As illustrated in Figure 3a and Supplementary Figure S6, the apparatus comprises two separate chambers connected by an inversely U-shaped oil skim with WOSs. The left chamber

contains a mineral oil/water mixture at a volume ratio of 1:2, mimicking the scenario of floating oil spills on water surfaces. During the tests, mineral oil is extracted from the left chamber and transported to the right chamber via the WOSs. The collected oil is then quantified using an electronic balance. To maintain a steady rate of oil recovery, an oil feedstock is supplied to keep a consistent height difference between the oil layers in both chambers (ΔH). The entire setup is covered with a 10-μm-thick polyethylene film to minimize convective heat losses. For all the tests conducted under solar illumination, the left chamber is covered by an aluminum foil to prevent extra solar heating.

Benefiting from the excellent light-absorbing capability, WOSs can efficiently absorb and convert solar energy to thermal energy under solar irradiation. The temperature distribution across the surface of the WOS-60 under 1-sun solar illumination is visualized by an infrared (IR) camera (Figure 3b). Figure 3c presents the temperature variations over time recorded at specific points identified in Figure 3b. The surface temperature on top of WOS-60 reaches equilibrium at 82℃ after 30 minutes. Furthermore, even at the end of the “legs”, a notable temperature of approximately 60℃ is observed. Such elevated temperatures play a crucial role in substantially reducing oil viscosity (Figure 3d), leading to improved oil recovery performance.

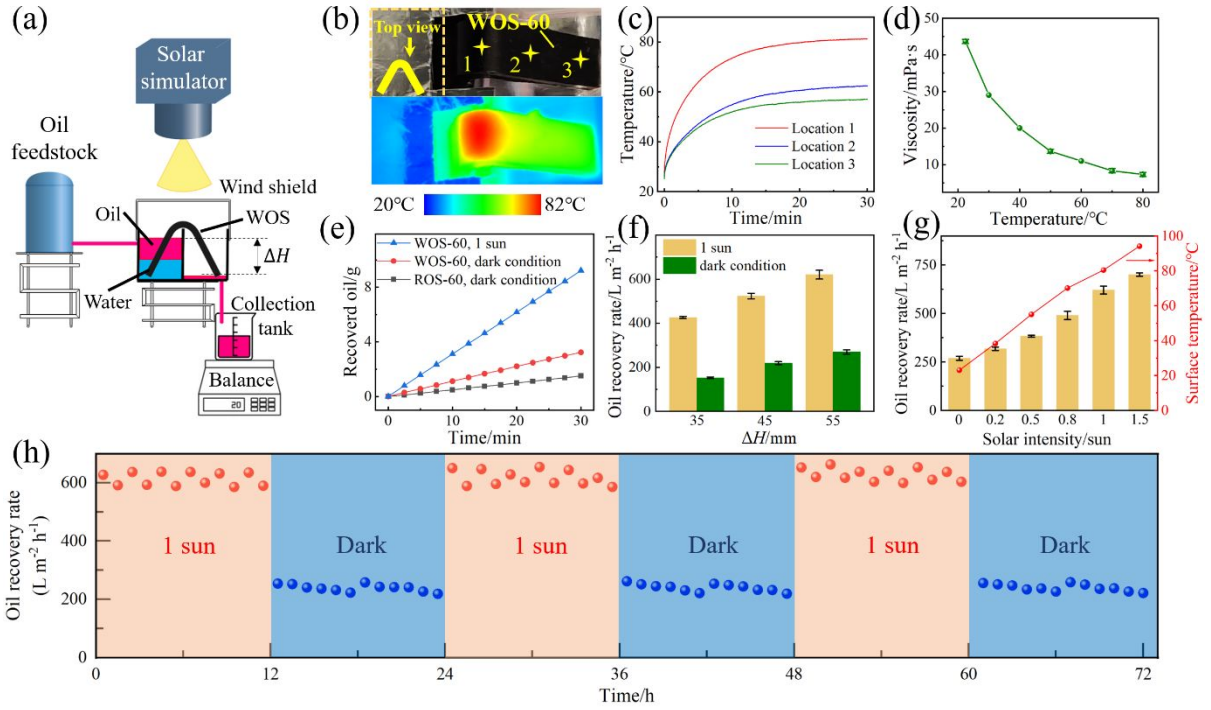

Figure 3. (a) Schematic illustration of the oil recovery setup with blue indicating water and red signifying mineral oil. (b) IR images showing the top-view surface temperature of WOS-60 operating under 1-sun irradiation after 30 min. (c) Temperature evolutions at the marked locations shown in (b). (d) Viscosity of mineral oil as a function of temperature. (e) Mass evolution of oil collected by WOS-60 and ROS-60. (f) Oil recovery rates of the WOS-60 under different ΔH. Error analysis was based on multiple repeat tests. (g) Oil recovery rates and surface temperatures of the WOS-60 working under different solar intensities. (h) Cyclic stability of the WOS-60 during a continuous 72-hour operation at a ΔH of 55 mm.

Figure 3e compares the oil masses recovered by WOS-60 and ROS-60 at a fixed ΔH of 35 mm. In dark conditions, WOS-60 shows superior oil recovery performance, achieving a rate of 152.5 L m^{-2} h^{-1}, which is approximately 2.6 times as high as the recovery rate (i.e., 61.7 L m^{-2} h^{-1}) of the ROS-60. Additionally, graphene-based membranes fabricated by another method, ambient drying, were tested and compared to the WOS-60 and ROS-60 samples. These ambient-dried oil skimmers feature hierarchical porous structures, with large pore sizes of several tens of microns and smaller pore sizes of several microns, as shown in Supplementary

Figure S7. This structural variation influences their oil recovery performance compared to the ROS samples, resulting in a lower oil recovery rate of 46.8 L m^{-2} h^{-1} under dark conditions (Supplementary Figure S7). When subjected to 1-sun solar irradiation, the rate of WOS-60 is boosted to 425.7 L m^{-2} h^{-1}, attributed to the decreased oil viscosity under the elevated temperature. The impact of the oil-to-water volume ratio on oil recovery performance is also investigated. We have tested the oil recovery performance of oil skimmers in oil/water mixtures at volume ratios of 1:1 and 1:4. The oil recovery rate remains relatively unchanged as the oil-to-water volume ratio varies (Supplementary Figure S8), which can be attributed to the consistent and fixed ΔH. Interestingly, increasing ΔH further amplifies the oil recovery rate, as the siphon mechanism is predominantly governed by shifts in gravitational potential energy[27,29]. As Figure 3f demonstrates, the oil recovery performance of WOS-60 augments in tandem with ΔH. Specifically, high rates of 269.1 L m^{-2} h^{-1} in dark conditions and 620.2 L m^{-2} h^{-1} under 1-sun irradiation are achieved at a ΔH of 55 mm. This performance not only surpasses that of previously reported siphon-based oil skimmers but also rivals that of other externally powered oil recovery apparatuses (Supplementary Table S1). Moreover, the oil/water mixture separation efficiency is calculated to be 99.92% (Supplementary Figure S9), illustrating the excellent capability of WOS-60 in effectively recovering oil from oil/water mixtures. Additional tests of oil transport under different solar irradiation intensities of 0.2, 0.5, 0.8, 1, and 1.5 suns are also conducted to systematically evaluate how decreased oil viscosity enhances the oil recovery performance of the WOS-60 skimmers. Meanwhile, the surface temperatures of the oil skimmers under different solar irradiation intensities are recorded. As demonstrated in Figure 3g and Supplementary Figure S10, the oil skimmers exhibit oil recovery rates of 318.1, 383.2,

489.9, 620.2, and 700.3 L m^{-2} h^{-1} at solar intensities of 0.2, 0.5, 0.8, 1, and 1.5 suns, respectively. The increase of oil recovery rate with solar intensity can be attributed to the more elevated surface temperatures induced by higher solar intensities. In addition, oil recovery tests based on a different type of oil with much higher viscosity (denoted as oil-II) and WOS-60 are conducted, as shown in Supplementary Figure S11. An average oil recovery rate of 111.4 L m^{-2} h^{-1} is achieved under dark conditions, which is increased to 270.7 L m^{-2} h^{-1} at 1 sun, indicating that oil-II can also be spontaneously and continuously recovered by WOS-60. Therefore, our proposed skimmers are effective in recovering oil with a broad range of viscosities.

To test the long-term stability of WOS-60, a continuous 72-hour oil recovery evaluation, alternating between 12 hours of sunlight exposure and 12 hours of darkness, was carried out. Throughout the test, collected oil was manually redirected to the feedstock at 2-hour intervals under sunlight and 6-hour intervals in darkness, ensuring a steady ΔH of 55 mm. Interestingly, oil recovery rate under both 1-sun irradiation and dark conditions remained consistent (Figure 3h), demonstrating the robust cyclic stability of WOS-60. We note that although residual oil remains within the skimmers after each oil recovery test, the oil skimmers are ready for next uses without performance degradation. As an illustration, after initial tests on fresh WOS-60s, the oil skimmers were stored under ambient conditions for two months. Upon re-evaluation of their oil recovery performance, as shown in Supplementary Figure S12, the oil recovery rates remained consistent with that of the fresh samples, and the separation efficiencies of the oil/water mixture were maintained at a high level of up to 99.85% (Supplementary Figure S9).

These results highlighted the excellent reusability and stability of the WOS-60s, demonstrating that the used membranes can remain free from secondary pollution under ambient environmental conditions.

2.3. Oil recovery performance of WOS with different connection angles

Our results indicate that the well-aligned channels in the two "legs" of WOS-60 significantly improve oil recovery performance compared to ROS-60. This raises two intriguing questions: First, how do the well-aligned channels in the two "legs" merge in the "head" region? Second, does the connection angle (denoted as θ) between these "legs" influence the channel structures established during the freeze-casting procedures, and, consequently, the oil recovery efficiency? To investigate these aspects, we fabricated WOSs and ROSs with various θ values ranging from 0° to 100° at a fixed ΔH of 35 mm. To eliminate the potential confounding influence of the solar-heating effect, oil recovery tests were conducted under dark conditions.

Figure 4a presents the comparative oil performance of ROSs with varying θ values. Notably, the oil recovery performance deteriorates progressively as θ increases. This decrement can be attributed to an increased channel resistance resulting from an extended flow pathway at larger θ values. Based on Bernoulli's equation[44], the velocity (v) of the outgoing oil from the skimmers can be represented as:

$$v = [2g(\Delta H - f_L)]^{1/2} \quad (1)$$

where g is the gravitational acceleration constant, and f_L represents the channel resistance,

which is described by[44]:

$$f_L \propto C \times L + \Delta P_{base} \quad (2)$$

where C is the pressure drop constant, L is the total flow distance of oil, and ΔP_{base} is the base pressure drop. Based on the relationship, an elongated oil flow distance clearly leads to a diminished oil recovery rate.

Figure 4b illustrates the temporal evolution of recovered mineral oil by WOSs for diverse θ values under dark conditions. Subsequently, the corresponding oil recovery rates for both ROSs and WOSs are calculated and depicted in Figure 4c. Interestingly, at a θ of 0°, the oil recovery rate of WOS is unexpectedly inferior to that of ROS. This suggests that the oriented channel structure within the two "legs" in WOS-0 fails to enhance its overall oil recovery efficiency. As θ increases from 0° to 60°, the oil recovery rate of WOSs display a pronounced increment, reaching a peak value of 152.5 L m^{-2} h^{-1} at $\theta = 60°$. Beyond this point, as θ continues to rise, a decline in the recovery rate is observed. However, the ratio of the oil recovery rate between WOSs and ROSs, denoted as v_{WOS}/v_{ROS}, consistently increases as θ augments.

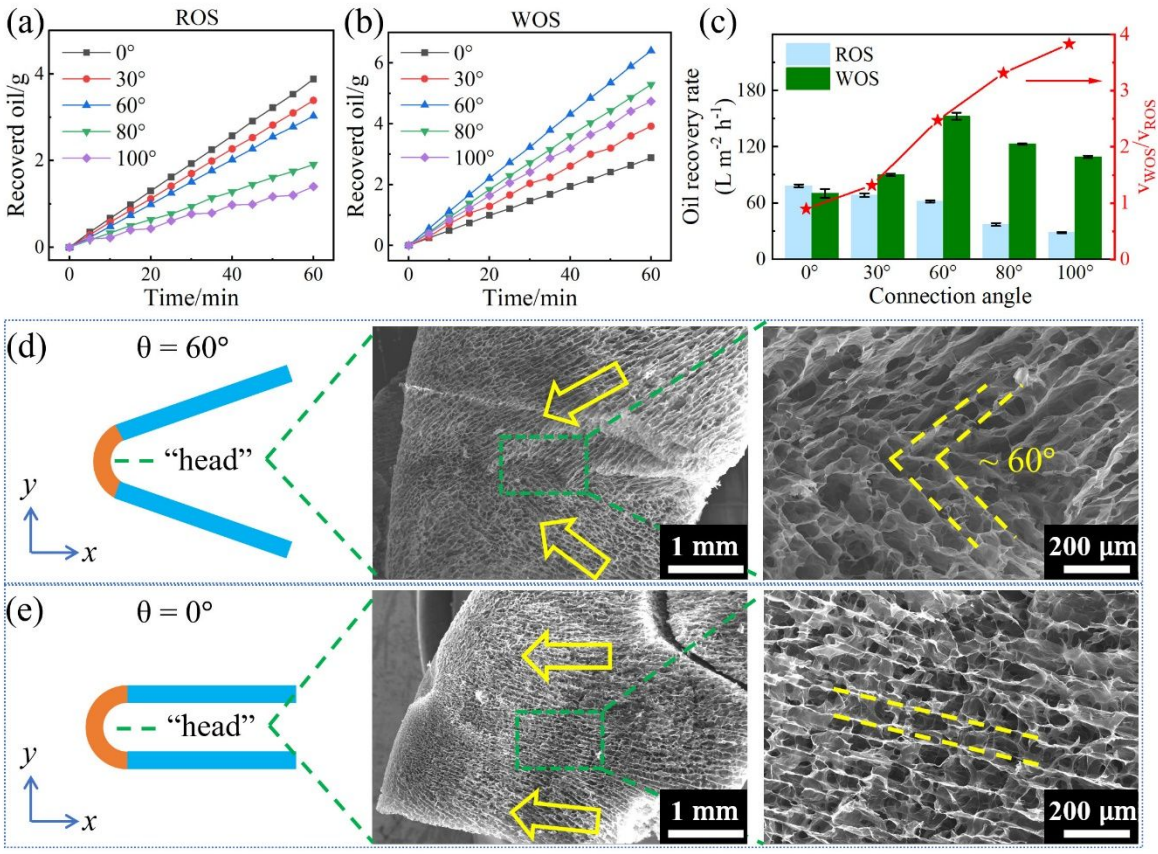

Figure 4. (a) Mass evolution of collected oil by ROSs with different θ under dark conditions. (b) Mass evolution of collected oil by WOSs with different θ under dark conditions. (c) Calculated oil recovery rates for ROSs and WOSs with different θ under dark conditions. (d-e) SEM images showing the channel structure in the "head" of (d) WOS-60 and (e) WOS-0. Yellow arrows denote the freezing direction during the freeze casting process.

To reveal the correlation between the oil recovery performance and θ of WOSs, the channel architecture at the "head" of WOS-60 (Figure 4d) was examined and compared with that of WOS-0 (Figure 4e), of which the connection angle (i.e., 0°) is typical in conventional siphon-assisted devices[27–29]. In WOS-60, the freezing directions within its two "legs" converge at an angle of 60°. This leads to a connected channel structure in the "head" region, with a connection angle of approximately 60° (Figure 4d). Consequently, this configuration enables

a low resistance to oil flow within the "head" of WOS-60 and thus enhances the overall recovery rate. In contrast, the freezing directions in both "legs" of WOS-0 run parallel to the *x*-direction, causing channels within its "head" to be orthogonal to the oil's flow direction (*y*-direction), as shown in Figure 4e. This structure significantly impedes oil movement across the "head" of WOS-0, thereby undermining the oil recovery rate compared to ROS-0 at $\theta = 0°$. As θ increases from 0° to 60°, the resistance for oil traversing the "head" region diminishes, leading to an enhanced oil recovery rate. However, for θ values over 60°, the elongated flow distance results in higher channel resistance, compromising the overall oil recovery performance. Even though oil flow resistance in the "head" region continues to decrease with larger θ (evidenced by the ascending WOS-to-ROS recovery rate ratio in Figure 4c), the recovery rate of WOSs decreases as θ progresses from 60° to 100°. Hence, WOS-60 with a θ of 60° is demonstrated to be the optimal configuration for oil recovery.

The morphology and structure of channels formed by freeze casting are intrinsically linked to the growth patterns of ice crystals[36,45]. The growth behavior of these crystals is influenced by the temperature gradient present in the liquid precursor during the solidification process. Importantly, ice crystals tend to grow following the direction of the imposed thermal gradient. To shed light on the formation of distinct channel structures in the "head" regions of WOS-60 and WOS-0, we monitored the real-time temperature distributions using a high-resolution IR camera (FLIR A600) with a 25-micron precision lens. Figure 5a shows the photograph of the "head" region in the freeze-casting mold for WOS-60, and Figures 5b-d present the sequential temperature distributions during solidification. In the initial phase of the

GO solution freezing within the "head" region (as shown in Figure 5b), the temperature gradients align with the directions of the two "legs" in the mold. As the freezing process advances, a consistent angle of approximately 60° is retained in the temperature gradients (Figure 5c), leading to the merging of freezing within the "head" region (Figure 5d). This phenomenon results in the formation of an interconnected framework of ice crystals that, upon sublimation, yields interconnected channels in the "head".

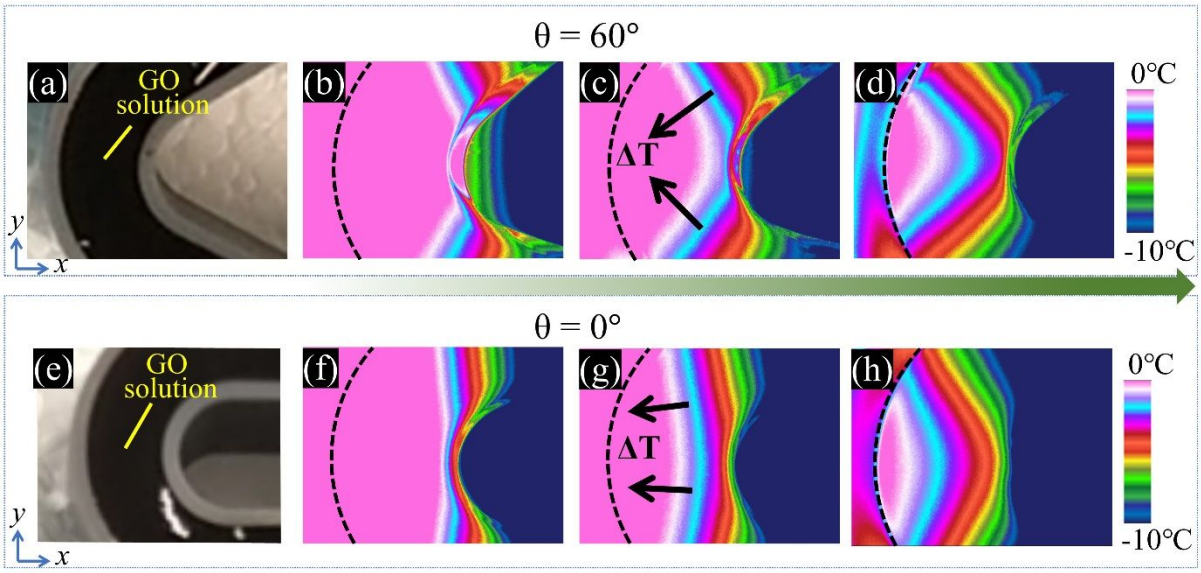

Figure 5. (a) Photograph of the "head" region of the directional freeze casting mold for WOS-60. (b-d) Evolution of temperature distribution during the freezing progression within the "head" region of the WOS-60 mold. (e) Photograph of the "head" region of the directional freeze casting mold for WOS-0. (f-h) Evolution of temperature distribution during the freezing progression within the "head" region of the WOS-0 mold. Dark arrows indicate the direction of the temperature gradient during freezing.

Contrarily, the freezing process in the WOS-0 mold (Figures 5e-h) shows a temperature gradient aligned solely in the *x*-direction right from the commencement of freezing in the "head" region. This orientation remains unchanged throughout the process, prompting the ice crystals

to grow in a unidirectional manner along the *x*-axis. Consequently, the channels formed after ice sublimation are well-aligned in the *x*-direction, impeding oil transport along the *y*-direction.

2.4. Outdoor oil recovery field tests

To gauge the oil recovery efficiency of the WOS-60 under realistic environmental conditions, we conducted outdoor field tests during a mostly sunny day in Richardson, Texas, U.S. (coordinates: 96.73°W, 32.95°N). Figure 6a depicts our experimental setup for outdoor oil recovery tests. We employed a pyranometer to measure the real-time incident solar flux (Figure 6b) and a weather station to record ambient temperatures (Figure 6c) and additional weather conditions (Supplementary Figure S13). During the tests, to stabilize ΔH at an approximate value of 55 mm, the collected oil was manually cycled back to the feedstock container every 1 hour during daylight and every 4 hours after sunset. The oil recovery rate of WOS-60, determined on an hourly basis, is presented in Figure 6d. During the noon hour (between 12:00 and 13:00), the WOS-60 exhibited an exceptionally high oil recovery rate, reaching a peak value of 938.2 L m^{-2} h^{-1} under an average solar flux of 923 W m^{-2}. This rate is significantly higher than that achieved under 1-sun irradiation in indoor experiments (i.e., 620.2 L m^{-2} h^{-1}). Additionally, the cumulative daily oil collection of WOS-60 reaches up to 14,001 L m^{-2}, corresponding to an annual yield of approximately 32,143 barrels m^{-2}. Note that the oil recovery performance could be further improved with a more substantial ΔH.

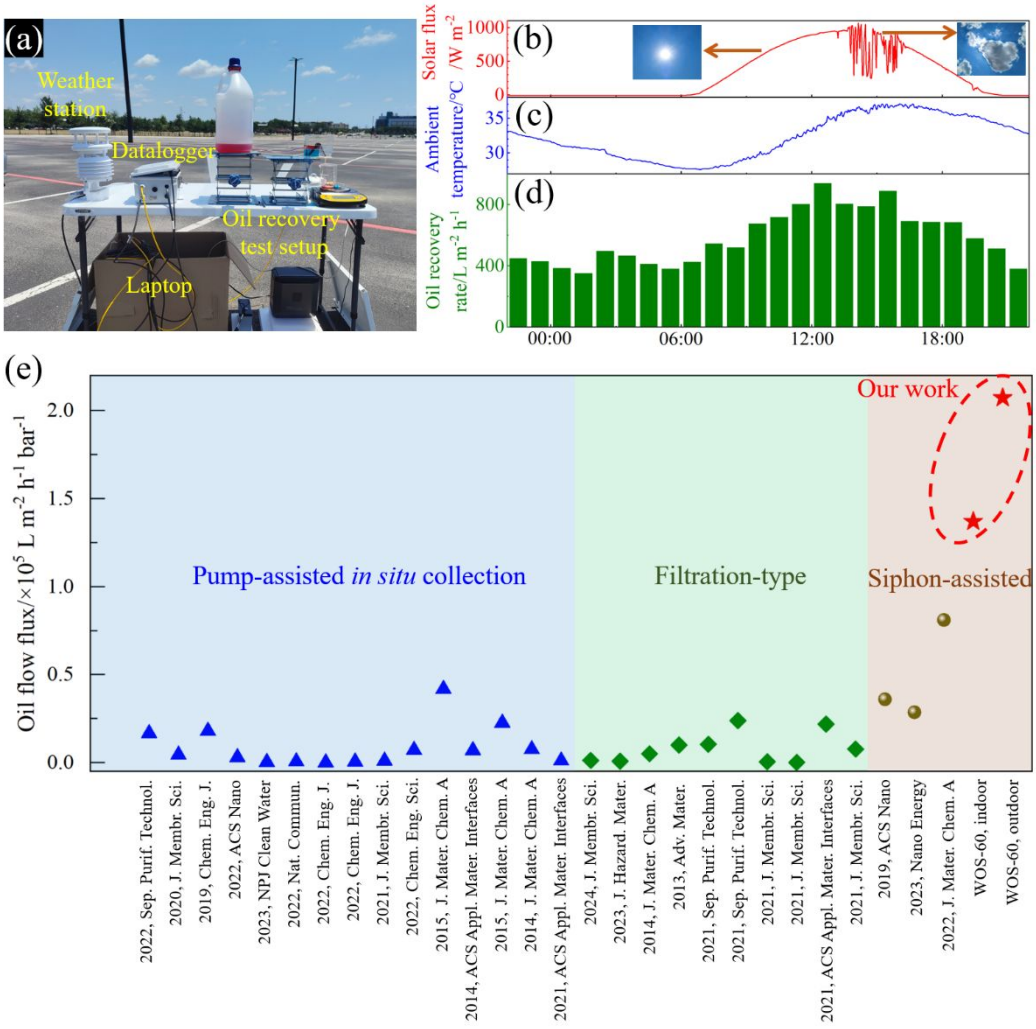

Figure 6. (a) Photograph of the experimental setup for outdoor oil recovery field tests. Measured (b) solar flux, (c) ambient temperature, and (d) oil recovery rate of the WOS-60 over time during the outdoor field test in Richardson, Texas, U.S. (22:00, June 25, 2023 to 22:00, June 26, 2023). (e) Comparative analysis of the oil flow flux for WOS-60 and other reported oil recovery devices.

To evaluate the oil recovery capability of WOS-60 in comparison to other types of oil skimmers, we determine the oil flow flux (q) through dividing the oil recovery rate (v) by the driving pressure (ΔP)[21,22]:

$$q = v/\Delta P \tag{3}$$

The driving pressure in the siphon-assisted system is given by[46]:

$$\Delta P = \rho_{oil} g \Delta H \quad (4)$$

where ρ_{oil} is the density of mineral oil, and g denotes the acceleration of gravity. As shown in Figure 6e, the WOS-60 exhibits excellent oil flow fluxes of 136,982 and 207,218 L m^{-2} h^{-1} bar^{-1} during the indoor and outdoor tests, respectively, significantly outperforming pump-assisted and other filtration-type oil recovery systems (Details are shown in Supplementary Table S1). Importantly, the WOS-60 operates autonomously and continuously without the requirement for external electricity or human intervention. The high operational efficiency of the oil skimmers assisted by siphon effects and renewable energy demonstrates great potential for practical oil spill recovery.

3. Conclusions

In summary, we have reported a novel LHFC technique to fabricate siphon-assisted oil skimmers and systematically assessed their self-pumping oil recovery performance in oil-contaminated wastewater. By tracking real-time temperature distributions, we determined that the connection angle between the two "legs" of WOSs could significantly affect the temperature gradient, subsequently impacting the channel formation within the "head". The optimal oil recovery performance was observed at a connection angle of 60°, which is the result of balancing the reduced transport barrier within the "head" against the augmented resistance in the "legs" due to the elongated flow pathway. Consequently, the WOS-60, benefiting from the well-aligned channel structure in the "legs" and interconnected pathways in the "head",

exhibits remarkable oil recovery performance compared to ROSs with an outstanding oil/water separation efficiency of 99.92%. During the indoor test, the oil recovery rates were measured to be 269.1 L m^{-2} h^{-1} in dark conditions and 620.2 L m^{-2} h^{-1} under 1-sun irradiation. Moreover, the rate reached a maxima value of 938.2 L m^{-2} h^{-1} at noon during an outdoor test, accumulating a daily oil collection of 14,001 L m^{-2} and an annual yield of 32,143 barrels m^{-2}. The oil flow flux is calculated to be 207,218 L m^{-2} h^{-1} bar^{-1}, significantly higher than the reported external power-driven oil recovery systems. Our research paves the way for innovative designs of channel structures with intricate shapes, showing great potential for rapid liquid transportation across diverse applications.

Supporting information

Detailed information on materials, synthesis and characterization of WOS and ROS; contact angle of oil droplet on WOS-60; SEM images of GPs grown on the surface of WOS-60; photograph showing the lab-scale oil recovery test setup; the viscosity of mineral oil as a function of temperature; details on water/oil separation efficiency calculations; additional weather conditions during the outdoor field test; comparison of oil recovery performance between the WOS-60 and reported oil recovery devices.

Acknowledgments

G.X. thanks the University of Texas at Dallas startup fund and the support from the NSF (Grant No. CBET-1949962). T.L. thanks the support from the NSF (Grant No. CBET-1949910).

Notes

The authors declare no conflicts of interest.

References

1. Bishop, R.C., Boyle, K.J., Carson, R.T., Chapman, D., Hanemann, W.M., Kanninen, B., Kopp, R.J., Krosnick, J.A., List, J., Meade, N., et al. (2017). Putting a value on injuries to natural assets: The BP oil spill. Science *356*, 253–254. 10.1126/science.aam8124.

2. Jernelöv, A. (2010). How to defend against future oil spills. Nature *466*, 182–183. 10.1038/466182a.

3. Wu, M., Shi, Y., Chang, J., Li, R., Ong, C., and Wang, P. (2018). Sunlight Induced Rapid Oil Absorption and Passive Room-Temperature Release: An Effective Solution toward Heavy Oil Spill Cleanup. Advanced Materials Interfaces *5*, 1800412. 10.1002/admi.201800412.

4. Ge, J., Zhao, H.-Y., Zhu, H.-W., Huang, J., Shi, L.-A., and Yu, S.-H. (2016). Advanced Sorbents for Oil-Spill Cleanup: Recent Advances and Future Perspectives. Advanced Materials *28*, 10459–10490. 10.1002/adma.201601812.

5. Zhu, Y., Wang, D., Jiang, L., and Jin, J. (2014). Recent progress in developing advanced membranes for emulsified oil/water separation. NPG Asia Materials *6*, e101–e101. 10.1038/am.2014.23.

6. Fu, Y., and Guo, Z. (2022). Natural polysaccharide-based aerogels and their applications in oil–water separations: a review. J. Mater. Chem. A *10*, 8129–8158. 10.1039/D2TA00708H.

7. Rasouli, S., Rezaei, N., Hamedi, H., Zendehboudi, S., and Duan, X. (2021). Superhydrophobic and superoleophilic membranes for oil-water separation application: A comprehensive review. Materials & Design *204*, 109599. 10.1016/j.matdes.2021.109599.

8. Xiang, B., Sun, Q., Zhong, Q., Mu, P., and Li, J. (2022). Current research situation and future prospect of superwetting smart oil/water separation materials. J. Mater. Chem. A *10*, 20190–20217. 10.1039/D2TA04469B.

9. Al-Majed, A.A., Adebayo, A.R., and Hossain, M.E. (2012). A sustainable approach to controlling oil spills. Journal of Environmental Management *113*, 213–227. 10.1016/j.jenvman.2012.07.034.

10. Fragoso ados Santos, H., Duarte, G.A.S., Rachid, C.T. da C., Chaloub, R.M., Calderon, E.N., Marangoni, L.F. de B., Bianchini, A., Nudi, A.H., do Carmo, F.L., van Elsas, J.D., et al. (2015). Impact of oil spills on coral reefs can be reduced by bioremediation using probiotic microbiota. Scientific Reports *5*, 18268. 10.1038/srep18268.

11. Motta, F.L., Stoyanov, S.R., and Soares, J.B.P. (2018). Application of solidifiers for oil spill containment: A review. Chemosphere *194*, 837–846. 10.1016/j.chemosphere.2017.11.103.

12. Cheng, M., Gao, Y., Guo, X., Shi, Z., Chen, J., and Shi, F. (2011). A Functionally Integrated Device for Effective and Facile Oil Spill Cleanup. Langmuir *27*, 7371–7375. 10.1021/la201168j.

13. Wang, F., Lei, S., Xue, M., Ou, J., and Li, W. (2014). In Situ Separation and Collection of Oil from Water Surface via a Novel Superoleophilic and Superhydrophobic Oil Containment Boom. Langmuir *30*, 1281–1289. 10.1021/la403778e.

14. Gu, J., Xiao, P., Chen, J., Liu, F., Huang, Y., Li, G., Zhang, J., and Chen, T. (2014). Robust preparation of superhydrophobic polymer/carbon nanotube hybrid membranes for highly effective removal of oils and separation of water-in-oil emulsions. J. Mater. Chem. A *2*, 15268–15272. 10.1039/C4TA01603C.

15. Ding, Y., Xu, S., Zhang, H., Zhang, J., Qiu, Z., Chen, H., Wang, J., Zheng, J., and Wu, J. (2021). One-Step Fabrication of a Micro/Nanosphere-Coordinated Dual Stimulus-Responsive Nanofibrous Membrane for Intelligent Antifouling and Ultrahigh Permeability of Viscous Water-in-Oil Emulsions. ACS Appl. Mater. Interfaces *13*, 27635–27644. 10.1021/acsami.1c05896.

16. Zhang, T., Xiao, C., Zhao, J., Liu, X., Ji, D., and Zhang, H. (2021). One-step facile fabrication of PVDF/graphene composite nanofibrous membrane with enhanced oil affinity for highly efficient gravity-driven emulsified oil/water separation and selective oil absorption. Separation and Purification Technology *254*, 117576. 10.1016/j.seppur.2020.117576.

17. Zhang, W., Shi, Z., Zhang, F., Liu, X., Jin, J., and Jiang, L. (2013). Superhydrophobic and Superoleophilic PVDF Membranes for Effective Separation of Water-in-Oil Emulsions with High Flux. Advanced Materials *25*, 2071–2076. 10.1002/adma.201204520.

18. Xiang, B., Gong, J., Sun, Y., Yan, W., Jin, R., and Li, J. (2024). High permeability PEG/MXene@MOF membrane with stable interlayer spacing and efficient fouling resistance for continuous oily wastewater purification. Journal of Membrane Science *691*, 122247. 10.1016/j.memsci.2023.122247.

19. Yu, J., Cao, C., and Pan, Y. (2023). A solar-driven degradation-evaporation strategy for membrane self-cleaning in the efficient separation of viscous crude oil/water emulsions. Journal of Hazardous Materials *457*, 131826. 10.1016/j.jhazmat.2023.131826.

20. Chen, X., Dai, C., Zhang, T., Xu, P., Ke, W., Wu, J., Qiu, M., Fu, K., and Fan, Y. (2022). Efficient construction of a robust PTFE/Al2O3 hydrophobic membrane for effective oil purification. Chemical Engineering Journal *435*, 134972. 10.1016/j.cej.2022.134972.

21. Yang, C., Long, M., Ding, C., Zhang, R., Zhang, S., Yuan, J., Zhi, K., Yin, Z., Zheng, Y., Liu, Y., et al. (2022). Antifouling graphene oxide membranes for oil-water separation via hydrophobic chain engineering. Nature Communications *13*, 7334. 10.1038/s41467-022-35105-8.

22. Cheng, X., Ye, Y., Li, Z., Chen, X., Bai, Q., Wang, K., Zhang, Y., Drioli, E., and Ma, J. (2022). Constructing Environmental-Friendly “Oil-Diode” Janus Membrane for Oil/Water Separation. ACS

Nano *16*, 4684–4692. 10.1021/acsnano.1c11388.

23. Zhang, X., Liu, C., Yang, J., Huang, X.-J., and Xu, Z.-K. (2021). Wettability Switchable Membranes for Separating Both Oil-in-water and water-in-oil emulsions. Journal of Membrane Science *624*, 118976. 10.1016/j.memsci.2020.118976.

24. Wang, J., He, B., Ding, Y., Li, T., Zhang, W., Zhang, Y., Liu, F., and Tang, C.Y. (2021). Beyond Superwetting Surfaces: Dual-Scale Hyperporous Membrane with Rational Wettability for "Nonfouling" Emulsion Separation via Coalescence Demulsification. ACS Appl. Mater. Interfaces *13*, 4731–4739. 10.1021/acsami.0c19561.

25. Ge, J., Shi, L.-A., Wang, Y.-C., Zhao, H.-Y., Yao, H.-B., Zhu, Y.-B., Zhang, Y., Zhu, H.-W., Wu, H.-A., and Yu, S.-H. (2017). Joule-heated graphene-wrapped sponge enables fast clean-up of viscous crude-oil spill. Nature Nanotechnology *12*, 434–440. 10.1038/nnano.2017.33.

26. Wu, M.-B., Huang, S., Liu, T.-Y., Wu, J., Agarwal, S., Greiner, A., and Xu, Z.-K. (2021). Compressible Carbon Sponges from Delignified Wood for Fast Cleanup and Enhanced Recovery of Crude Oil Spills by Joule Heat and Photothermal Effect. Advanced Functional Materials *31*, 2006806. 10.1002/adfm.202006806.

27. Wu, S., Tian, S., Jian, R., Wu, T.-N., Milazzo, T.D., Luo, T., and Xiong, G. (2022). Graphene petal foams with hierarchical micro- and nano-channels for ultrafast spontaneous and continuous oil recovery. J. Mater. Chem. A *10*, 11651–11658. 10.1039/D2TA00019A.

28. Wu, S., Jian, R., Tian, S., Zhou, L., Luo, T., and Xiong, G. (2023). Simultaneous solar-driven seawater desalination and continuous oil recovery. Nano Energy *107*, 108160. 10.1016/j.nanoen.2022.108160.

29. Wu, S., Yang, H., Xiong, G., Tian, Y., Gong, B., Luo, T., Fisher, T.S., Yan, J., Cen, K., Bo, Z., et al. (2019). Spill-SOS: Self-Pumping Siphon-Capillary Oil Recovery. ACS Nano *13*, 13027–13036. 10.1021/acsnano.9b05703.

30. Narayanamurthy, V., Jeroish, Z.E., Bhuvaneshwari, K.S., Bayat, P., Premkumar, R., Samsuri, F., and Yusoff, M.M. (2020). Advances in passively driven microfluidics and lab-on-chip devices: a comprehensive literature review and patent analysis. RSC Adv. *10*, 11652–11680. 10.1039/D0RA00263A.

31. Wang, P., Yuan, S., Yang, N., and Oppong, P.K. (2021). A comprehensive review on non-active micro-pumps for microfluidic platforms. Journal of Micromechanics and Microengineering *31*, 093001. 10.1088/1361-6439/ac1452.

32. Shao, G., Hanaor, D.A.H., Shen, X., and Gurlo, A. (2020). Freeze Casting: From Low-Dimensional Building Blocks to Aligned Porous Structures—A Review of Novel Materials, Methods, and Applications. Advanced Materials *32*, 1907176. 10.1002/adma.201907176.

33. Liu, H., Jiang, J., and Zhai, W. (2022). Bubble freeze casting artificial rattan. Chemical Engineering Journal *449*, 137870. 10.1016/j.cej.2022.137870.

34. Wu, S., Tian, S., Jian, R., Zhou, L., Luo, T., and Xiong, G. (2023). Bio-inspired salt-fouling resistant graphene evaporators for solar desalination of hypersaline brines. Desalination *546*, 116197. 10.1016/j.desal.2022.116197.

35. Chan, K.-Y., Shen, X., Yang, J., Lin, K.-T., Venkatesan, H., Kim, E., Zhang, H., Lee, J.-H., Yu, J., Yang, J., et al. (2022). Scalable anisotropic cooling aerogels by additive freeze-casting. Nature Communications *13*, 5553. 10.1038/s41467-022-33234-8.

36. Shahbazi, M.-A., Ghalkhani, M., and Maleki, H. (2020). Directional Freeze-Casting: A Bioinspired Method to Assemble Multifunctional Aligned Porous Structures for Advanced Applications. Advanced Engineering Materials *22*, 2000033. 10.1002/adem.202000033.

37. Scotti, K.L., and Dunand, D.C. (2018). Freeze casting – A review of processing, microstructure and properties via the open data repository, FreezeCasting.net. Progress in Materials Science *94*, 243–305. 10.1016/j.pmatsci.2018.01.001.

38. Cheng, Q., Huang, C., and Tomsia, A.P. (2017). Freeze Casting for Assembling Bioinspired Structural Materials. Advanced Materials *29*, 1703155. 10.1002/adma.201703155.

39. Wu, S., Xiong, G., Yang, H., Gong, B., Tian, Y., Xu, C., Wang, Y., Fisher, T., Yan, J., Cen, K., et al. (2019). Multifunctional Solar Waterways: Plasma-Enabled Self-Cleaning Nanoarchitectures for Energy-Efficient Desalination. Advanced Energy Materials *9*, 1901286. 10.1002/aenm.201901286.

40. Wu, S., Xiong, G., Yang, H., Tian, Y., Gong, B., Wan, H., Wang, Y., Fisher, T.S., Yan, J., Cen, K., et al. (2019). Scalable Production of Integrated Graphene Nanoarchitectures for Ultrafast Solar-Thermal Conversion and Vapor Generation. Matter *1*, 1017–1032. 10.1016/j.matt.2019.06.010.

41. Xu, C., Bo, Z., Wu, S., Wen, Z., Chen, J., Luo, T., Lee, E., Xiong, G., Amal, R., Wee, A.T.S., et al. (2020). Vertical graphene nano-antennas for solar-to-hydrogen energy conversion. Solar Energy *208*, 379–387. 10.1016/j.solener.2020.07.069.

42. Kong, Y., Dan, H., Kong, W., Gao, Y., Shang, Y., Ji, K., Yue, Q., and Gao, B. (2020). Self-floating maize straw/graphene aerogel synthesis based on microbubble and ice crystal templates for efficient solar-driven interfacial water evaporation. J. Mater. Chem. A *8*, 24734–24742. 10.1039/D0TA07576K.

43. Tian, S., Zhou, L., Wu, S., Jian, R., Keewan, A., Cui, S., and Xiong, G. (2022). Multifunctional superelastic graphene aerogels derived from ambient-dried graphene oxide/camphene emulsions. Materials Letters *328*, 133128. 10.1016/j.matlet.2022.133128.

44. Jeong, G.S., Oh, J., Kim, S.B., Dokmeci, M.R., Bae, H., Lee, S.-H., and Khademhosseini, A. (2014). Siphon-driven microfluidic passive pump with a yarn flow resistance controller. Lab Chip *14*, 4213–4219. 10.1039/C4LC00510D.

45. Dong, X., Chua, B.W., Li, T., and Zhai, W. (2022). Multi-directional freeze casting of porous ceramics with bone-inspired microstructure. Materials & Design *224*, 111344. 10.1016/j.matdes.2022.111344.

46. Huang, S., Song, J., Lu, Y., Lv, C., Zheng, H., Liu, X., Jin, Z., Zhao, D., Carmalt, C.J., and Parkin, I.P. (2016). Power-free water pump based on a superhydrophobic surface: generation of a mushroom-like jet and anti-gravity long-distance transport. J. Mater. Chem. A *4*, 13771–13777. 10.1039/C6TA04908G.